# Ductile crack initiation and growth on a plasticized Polyvinylchloride during air bag deployment

Lucien Laiarinandrasana[1], Clément Bertaux[1], Nicolas Amouroux[2], and Cristian Ovalle Rodas[1]

[1] MINES ParisTech, PSL University, MAT - Centre des Matériaux, CNRS UMR 7633, BP 87 91003 Evry, France
[2] Westlake Global Compounds, 1bis rue Maurice Hollande, 51100 Reims, France

With the goal of ensuring the security of passengers for automotive industry, the present work addresses the ductile fracture process of plasticized Polyvinylchloride (PVC). Dedicated clamped single edge notch bending (SENB) specimens were used to characterize the mechanisms of crack initiation and propagation for the studied material. The exploitation of the experimental database associated with finite element simulation of the crack propagation allowed, on the one hand, the calibration factor $\eta_p$ of this specific SENB specimen to be established, as a function of the crack depth ratio. On the other hand, the fracture toughness of the studied plasticized PVC was estimated to be $10.8\,\text{kJ/m}^2$, value which was close to that reported in the literature for modified PVC. By using this fracture toughness value, a methodology aiming at the prediction of ductile crack initiation of the PVC skin integrated into a real dashboard (full scale test) was proposed.

**Keywords:** fracture mechanics, impact strength, polymers, ductile failure, finite elements

## 1 Introduction

The correct deployment of airbag spreading is a major concern for the security of passengers in the automotive industry. The design and elaboration of the dashboard is one of the key features for obtaining the required specifications. Plasticized Polyvinylchloride (PVC) skins are commonly used for the top surface of the three layers of the dashboard.

To assess the role of the system in the spreading of the airbag, full scale tests have been carried out at various temperatures. Figure 1 illustrates salient results of these tests which allow a better analysis of the deformation and failure of the opening of windows on the airbag box during deployment. The grid cell size was about 10 mm in the initial undeformed state, see Figure 1(a). From these tests, the following can be said.

- At 23 °C, see Figure 1(b), a net ductile tearing of the skin, following the scoring direction and accompanied by the deformation of the top surface of the airbag box, was observed. This is the desired fracture process. Using a Digital Image Correlation (DIC) software solution, the impact speed applied to the PVC skin was estimated to be 25 m/s.

- At −35 °C, see Figure 1(c), and the same impact speed as above, a brittle failure of the skin occurred with small deformations. The main crack was on the surface plane and followed the direction of the inner score already made on the plasticized PVC outer skin. The presence of secondary transverse cracks could be noticed. These may provoke fragmentation (Cox and Robertson 2007) of the dashboard, accompanied by the projection of the pieces of the material and so would be dangerous for the passengers.

- At 85 °C, see Figure 1(d), at the same impact speed, a significant deformation of the box together with an extreme extension of the skin delayed the opening time, if it occurred, as ballooning could prevent the opening of the box. This situation is the most dangerous condition which needs to be avoided even though the ultimate failure could also be qualified as ductile.
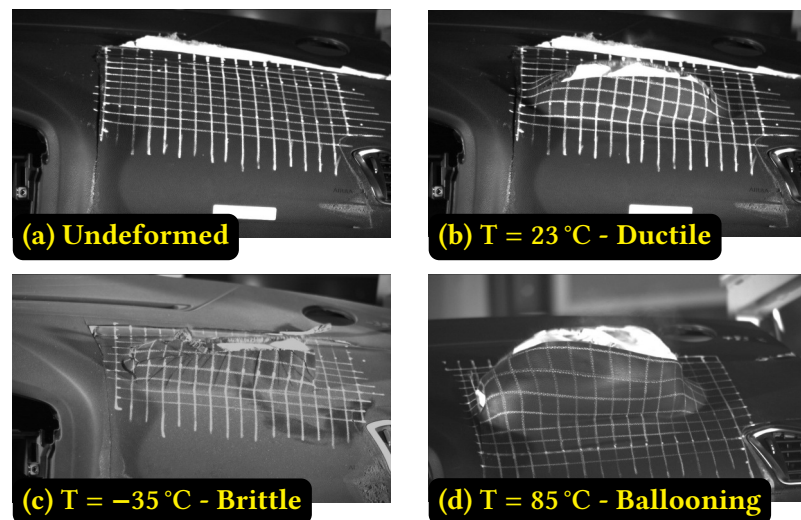
**Figure 1**    Tests at full scale of an air-bag deployment. (a) Undeformed state of the airbag window. (b) Correct ductile tearing at 23 °C. (c) Brittle failure at −35 °C where secondary transverse cracks can be observed. (d) Ballooning effect at 85 °C inducing delay or non opening.

Full scale experiments, as reported above, are very costly. Therefore, a research program was elaborated to directly test the plasticized PVC skin (Bertaux et al. 2021). One grade of plasticized PVC was selected, the most common one in the automotive industry. PVC skin plates were provided by the Westlake Global Compounds company. Scoring was added as a pre-crack on the samples using a robot for better reproducibility. The desired ratio between the score depth and the total thickness was about 0.5.

Standardized Charpy tests (ISO 179-1:2010 2010; ASTM D6110-18 2018) are commonly recommended to characterize the failure of plastics by impact. They enable the determination of the impact strength of the material by utilizing notched specimen with precise notch root radius. In the present work, the robot cut induced more acute crack with a notch root radius tending to zero. Moreover, the knowledge of the impact strengths allows the classification of plastics regarding their brittle fracture behaviour. As the desired failure mode is the ductile one for the plasticized PVC under study, this constitutes a limitation for the use of Charpy tests. Indeed, for very ductile plastics, the specimen may not fail after the impact. In this extreme case of no failure, the impact strength cannot be determined. Additionally, as mentioned above (test at 85 °C), this is the most dangerous situation. The aim of this work is then to characterize the ductile failure of the plasticized PVC by using fracture mechanics tools.

To achieve this goal, the present paper starts by recalling previous results (Bertaux et al. 2021) where the domain of interest, in terms of temperatures and impact speeds that emphasizes the ductile failure of the material, has been determined. Then, the methods used are described in the second section. The design of an experimental setup adapted to the material so as to obtain ductile failure characteristics is developed. The load parameters and the failure criteria for ductile fracture of polymers proposed by fracture mechanics theory (Williams 2001; Hale and Ramsteiner 2001) are introduced. The Finite Element analysis allowing the computation of the load parameters for complex cracked geometries is described at this stage. The section listing the results follows, starting from the specific mechanisms of crack initiation and growth, proper for the studied plasticized PVC. The fracture toughness of the material was determined by taking these mechanisms into account. The relationship between the obtained fracture toughness and the impact strength is then established. The last part of the paper consists of a set of discussions that propose a methodology to predict the ductile crack initiation on the PVC skin integrated into the dashboards thanks to the knowledge of the fracture toughness of the material.

## 2   Background

Impact tests were carried out using an Instron CEAST 9350 drop tower impact system (ISO 6603-2:2000 2000). The samples, consisting of thin and soft plates, had to be gripped along a

circular section. Details of the CEAST 9350 machine are provided by Bertaux et al. (2021). About one hundred test results have been analysed, corresponding to three tests for each selected test temperature ($-6$, $-3$, $0$, $5$, $10$, $15$, $20$, $25\,°C$) and each selected impact speed ($2$, $4.4$, $6$, $10\,m/s$).

The load versus deflection curves for the three tests at $20\,°C$ and at an impact speed of $4.4\,m/s$ are shown in Figure 2. A first loading stage was observed up to a load of about $650\,N$. Then, a
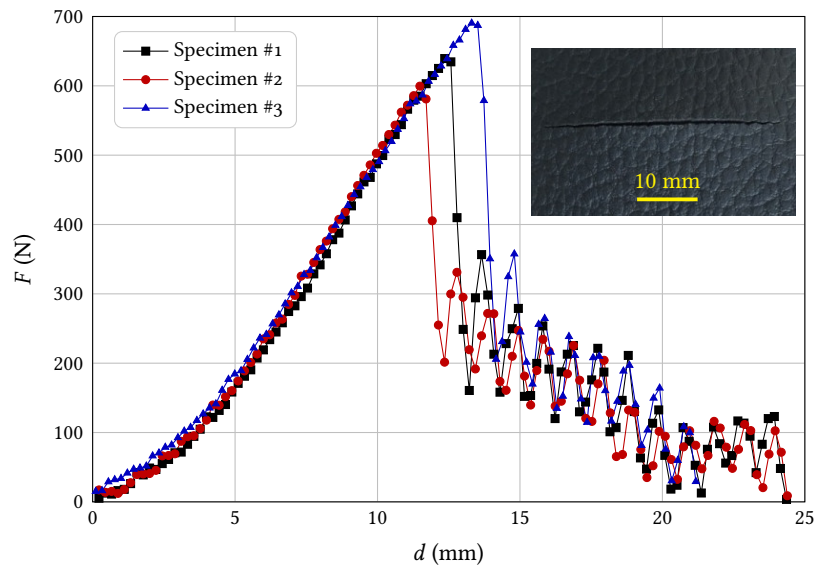


**Figure 2**   Load $F$ versus deflection $d$ for scored thin plates tested at $4.4\,m/s$ and $20\,°C$. Ductile fracture surface at the macroscopic scale is shown.

first load drop appeared followed by a gradual decrease with apparent oscillations. The slope of the first drop appeared to be same for the three tests. Additionally, the fracture surfaces of the tested samples exhibited characteristics of ductile failure.

From the load versus deflection curves, four main characteristic mechanical parameters were deduced.

- The stiffness of the system that corresponded to the slope of the linear part of the curve $\Delta F/\Delta d$ where $F$ is the load and $d$ is the deflection.
- The deflection and the load at failure, respectively $d_F$ and $F_F$, related to the last point before the abrupt drop of the load, *i.e.* at the onset of failure.
- The fracture energy $A_F$ determined by integration of the area under the load as a function of the deflection, up to $(d_F, F_F)$, that is

$$A_F = \sum_{i=1}^{F} \frac{(F_i + F_{i-1})}{2}(d_i - d_{i-1}). \tag{1}$$

The so-called impact strength here consisted in relating the fracture energy in Equation (1) to the fracture surface area $\Phi(t - a)$ where $\Phi$ is the diameter of the hemispherical impactor, $t$, the thickness of the skin, and $a$, the crack depth. In fact, this operation consisted of integrating the area under the net stress versus the deflection curve; the net stress being the ratio of the load per unit of the fractured surface.

The evolution of the impact strength of the studied plasticized PVC for the impact speed of $4.4\,m/s$ as a function of the test temperature is shown in Figure 3. Attention should be paid here to the upper shelf corresponding to the ductile mechanisms of failure. Under these test conditions, it could be concluded that the impact strength of the plasticized PVC was about $0.25\,kJ/m^2$.

The extension of this result to the other impact speeds was assessed by determining how the Ductile Failure Threshold Temperature $T_{dth}$ depends on the impact speed, as illustrated in Figure 4. Although the impact speed of $25\,m/s$ was not reached in this study, this plot indicates that $T_{dth}$ tended to stabilize and would be lower than $20\,°C$. This has been confirmed by the ductile failure obtained for the full scale test at $23\,°C$ shown in Figure 1(b).

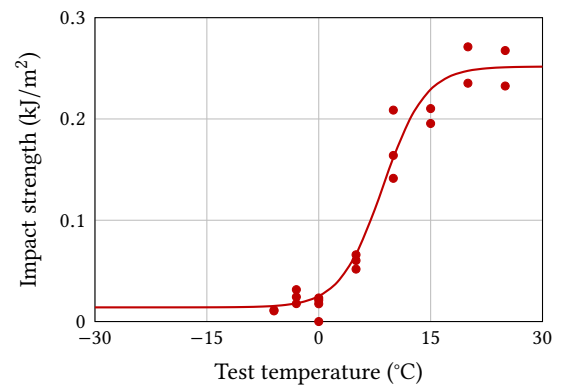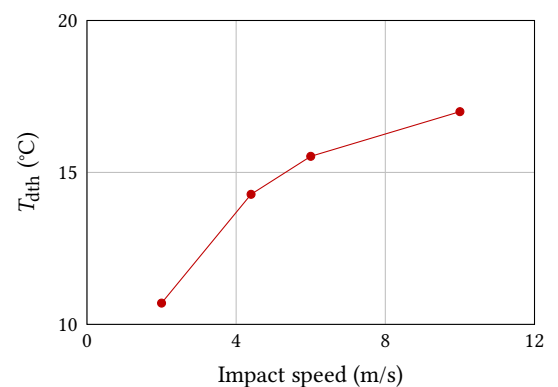**Figure 3**    Impact strength with respect to the test temperature.



**Figure 4**    Temperature to ductile fracture threshold $T_{dth}$ as a function of the impact speed.



Theoretically, the impact strength value of $0.25 \, \text{kJ/m}^2$ determined on the upper shelf does not depend on the impact speed. On the other hand, for pre-cracked specimens, the relationship between the impact strength and the fracture toughness has been investigated in several research papers on metals (Tanguy et al. 2006). The present work aims at the determination of the fracture toughness of the investigated plasticized PVC using the fracture mechanics approach.

## 3  Methods

### 3.1  Experiments

PVC skin plates of $90 \, \text{mm} \times 90 \, \text{mm}$ size and with $(1.2 \pm 0.1) \, \text{mm}$ thickness were provided by the Westlake Global Compounds company. Scoring was added as a pre-crack on the plates using a robot for better reproducibility. The desired ratio between the score depth and the total thickness was about 0.5. The robot cut the material so as to keep a retentive ligament thickness of $0.6 \, \text{mm}$. This implied an uncertainty on the crack depth ratio due to the real thickness of the skin and the roughness of the pattern on its top surface. Rectangular specimens were then machined from the scored thin plates, using a punch purposely assembled for better dimension reproducibility. The main dimensions of these rectangular scored samples were $90 \, \text{mm}$ in length and $29.8 \, \text{mm}$ in width. They mimic the fracture mechanics Single Edge Notch Bending (SENB) specimens for rigid plastics. The initial contact between the impactor and the sample constituted the major difference from the above mentioned CEAST test and the present experiments: a point and a line, respectively for the hemispherical impactor of CEAST and for the present SENB-like specimen.

To better understand the mechanisms of ductile crack initiation and propagation near the impacted zone of the scored thin sample, SENB specimens were tested using a Instron 5982 (up to $100 \, \text{kN}$ force capacity), with an additional and adapted load cell of $1 \, \text{kN}$. Figure 5(a) illustrates the top view of the experimental setup where span "S" of the rollers was fixed at $30 \, \text{mm}$. Moreover, the impactor pin and the rollers had the same root radius of $2 \, \text{mm}$. The plasticized PVC being extremely soft and flexible, unlike the classical SENB setup, specific jaws were designed to prevent any sample displacement during the test. It should be mentioned that the same boundary conditions were applied for the impact tests of pre-cracked thin plate. The data collected during the test consisted of the load and the corresponding deflection.

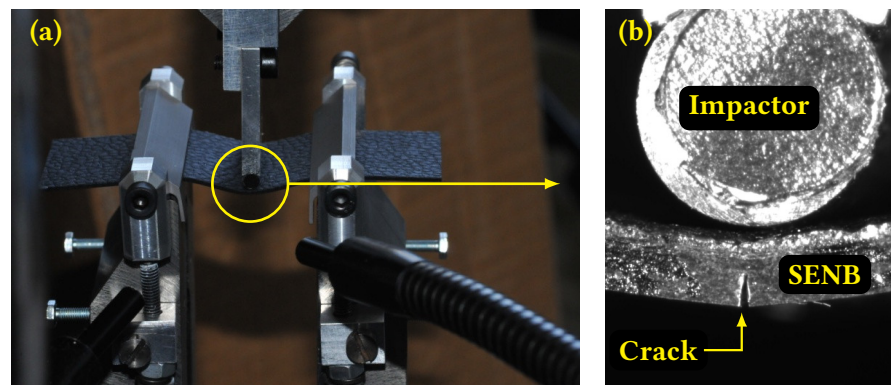Figure 5(b) details the region near the crack tip in the undeformed state. A video camera

**Figure 5**    Experimental setup for the clamped Single Edge Notch Bending test. (a) Top view where the patterns on the top skin of plasticized PVC plate can be observed. (b) Details of the non deformed crack tip.

was placed in front of one of the side surfaces so as to synchronize the load and the deflection recorded with the crack opening displacement and the advance of the crack. Due to the large strain experienced by the material, the camera had to be motorized to follow the position of the sample. The test deflection speed, of about 6 mm/s, was selected to match that of the motor.

### 3.2    Load parameters & Failure criteria

The fracture mechanics approach uses the concept of load parameter and failure criterion. The load parameter is the relevant variable combining the applied load and the characteristic lengths of the crack and the cracked body. The failure criterion consists of the critical value of the aforementioned variable (Williams 2001; Hale and Ramsteiner 2001; Baldi et al. 2013; Agnelli et al. 2015; Baldi et al. 2020).

The present work focuses on two load parameters: (1) a kind of fractured surface energy density, denoted $\Gamma$, corresponding to the area under the load–deflection curve, see Equation (1), related to the area of the remaining ligament, and (2) the J-integral recommended by the non linear fracture mechanics. The two corresponding failure criteria are the impact strength $\Gamma_c$ (Tanguy et al. 2006; Bohme and MacGillivray 1996) and the fracture toughness $J_c$, respectively.

#### 3.2.1    Fractured surface energy density

The fractured surface energy density stemming from the load and the deflection that have been measured during the test can be written as

$$\Gamma = \frac{A(F, d)}{B(W - a)} \tag{2}$$

with $A(F, d)$, the area under the load–deflection curve, $B$, the thickness of the specimen[1], $W$, the width of the specimen, and $a$, the crack depth.

For dedicated Charpy notched specimen, the critical surface energy density at failure (maximum load) corresponds to the impact strength of the material. Here, although a sharp crack is considered, $\Gamma_c$ will be considered as the impact strength. The evolution of the $\Gamma$ parameter with respect to the deflection should be analyzed so as to better understand the limits of this key parameter for an engineering approach.

#### 3.2.2    J-integral

In fact, for pre-cracked specimens, the curve to be analysed should be the load versus the Crack Opening Displacement (COD). The latter is more local than the deflection. However, its measurement was not easy as it came from video acquisition. The area under this curve is known

---

[1]    In the present study, in line with the commonly used terminology of the fracture mechanics, the thickness $B$ and the width $W$ of the specimen, in Equation (2) and Equation (3), correspond to the width and the thickness, respectively, of the machined rectangular specimens.

to be related to the J-integral, load parameter recommended in non-linear fracture mechanics analysis (Williams 2001; Hale and Ramsteiner 2001)

$$J_t = \eta_e \frac{A_e(F, \text{COD})}{B(W - a)} + \eta_p \frac{A_p(F, \text{COD})}{B(W - a)},$$ (3)

with $B$, the thickness of the specimen, $\eta_e$ and $\eta_p$, respectively the elastic and plastic calibration factors dependent on the crack depth ratio, the geometry of the specimen and the type of test. According to Williams (2001), this factor is assumed to be constant and equal to 2 for classical SENB geometry. For the present clamped SENB specimen, these factors are unknown. The elastic and plastic areas under the load–crack opening displacement curve are $A_e(F, \text{COD})$ and $A_p(F, \text{COD})$, respectively. The partition between these areas can be obtained once the linear correction of the load–COD curve (Hale and Ramsteiner 2001) had been operated.

For the sake of simplicity, many studies for polymer materials utilized only the plastic part

$$J_p = \eta_p \frac{A_t(F, \text{COD})}{B(W - a)}$$ (4)

of the J-integral (Williams 2001), where $A_t(F, \text{COD})$ is now the total energy corresponding to the total area under the load–crack opening displacement curve. The critical value (at the maximum load) is defined as the fracture toughness of the material (Laiarinandrasana et al. 2012; Bulloch 2004). For impact speed, the fracture toughness is described by Macgillivray (2001). It is worth noting that Equation (2) and Equation (4) differ in the $\eta_p$ factor and the relationship between the deflection and the notch opening displacement.

### 3.3   Finite Elements

Clamped SENB specimens tests were simulated using an in-house Finite Element (FE) code: the Z-set suite computing solution (http://zset-software.com/). The FE computation used 2D iso-parametric plane strain elements with reduced integration. Only half of the specimen was meshed. Figure 6(a) illustrates the meshes for the PVC sample, the impactor and the roller. Near the crack tip, the meshes were refined, see Figure 6(b), so as to obtain an element side of 50 μm at the crack tip.

The loading was controlled by the displacement of the impactor during the test (deflection). The numerical approach used here did not intend to predict the failure of the specimen but dealt with a FE simulation of the crack propagation by imposing the history of the crack extension included in the experimental data from video camera acquisition. An attempt was then made to simulate the crack initiation and growth using the "release nodal degree of freedom" (rndof) technique (Laiarinandrasana et al. 2006; Marcellan et al. 2019). This was achieved numerically by releasing gradually the nodes (in six steps for three quadratic elements) from the initial to the final remaining ligament, following the crack growth rate obtained experimentally.

The Z-set optimizer routine was first utilized to obtain a set of material coefficients using data from the load versus crack opening displacement curves. Then, the J-integral values with a propagating crack were computed using the de Lorenzi technique (de Lorenzi 1982). The comparison of these values to those of Equation (4) allowed to estimate the $\eta_p$ calibration factor.

## 4   Results

The upper shelf impact strength was of key interest for engineering structures such as the skin of the dashboard. It was estimated to be 0.25 kJ/m$^2$ from macroscopic data: the load and the deflection. In this section, attention will be paid to the quasi-static tests (ductile fracture) carried out on clamped SENB specimens at room temperature $T = 23\,°C$ and with an impact speed of 6 mm/s.

Figure 7 illustrates the side view of a deformed sample obtained from the video camera. The transverse cylindrical impactor moved down allowing the opening of the scored line. From this test, the load, the crack opening displacement and the crack extension ($\Delta a$) at the lateral surface were synchronized thanks to the embarked video–camera system. From this viewgraph, a large extension of the remaining ligament, leading to a crack tip opening displacement with an order of
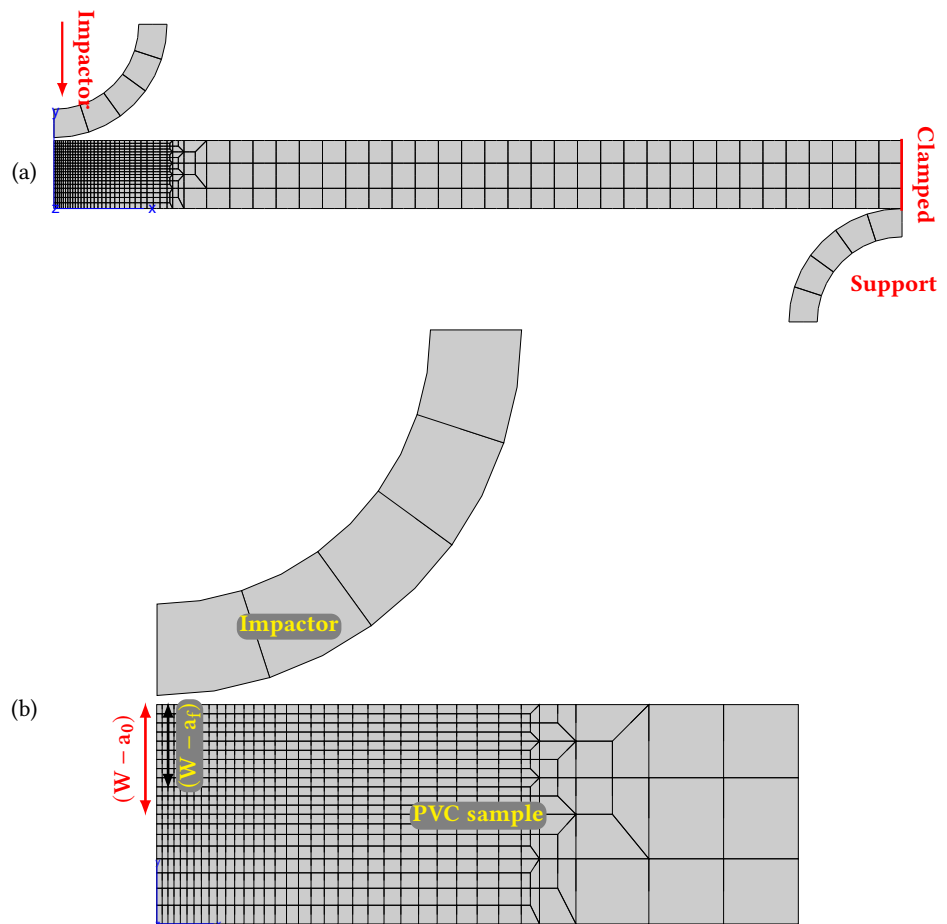
**Figure 6**   Mesh of the clamped SENB specimen. (a) Side view of the half specimen. (b) Details of the crack tip region (refined meshes). The size of refined mesh is 50 μm so that $a_0 - a_f = 150$ μm corresponds to the maximum crack extension before brittle failure.
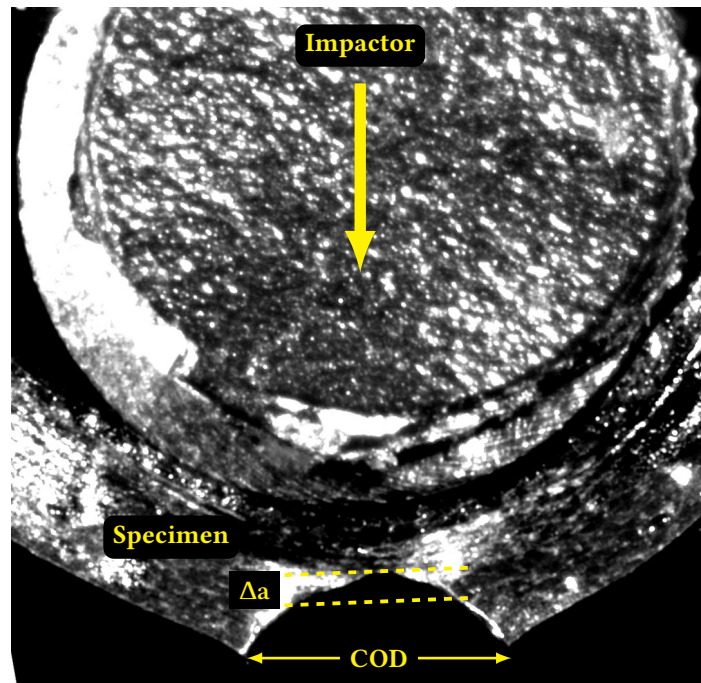


**Figure 7**   Details of the blunted crack tip during the deformation; measurements of the Crack Opening Displacement and the crack extension ($\Delta a$).

magnitude larger than the crack extension, was observed. At this deformed state, $\Delta a$ and COD measurements were relative. They might be subjected to uncertainties.

## 4.1 SENB experimental data

The thinness and softness of the plasticized PVC material made it difficult to perform the tests. For reproducibility purposes, seven tests were carried out with the same loading conditions. Only three of them were selected here since their reliability was considered as correct.

### 4.1.1 Crack Opening Displacement

The aim of Figure 8 is the analysis of the implication of the Crack Opening Displacement measurements to the classical load–deflection curve in Figure 8(a). The experimental data were

**Figure 8**  Experimental data obtained from quasi-static test on clamped SENB specimen at room temperature.
(a) Load versus deflection, (b) crack opening displacement COD versus deflection, and (c) ratio between the deflection and the COD.
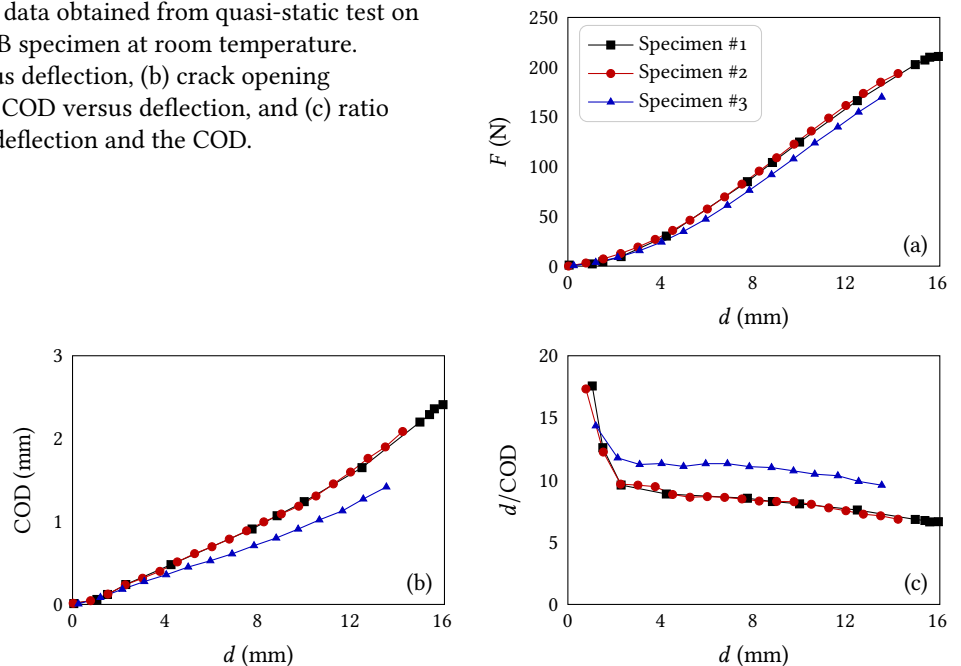


obtained from the three clamped SENB specimens with respect to the deflection. In Figure 8(a), the initial inflexion was due to the gradual compression applied to the scored thin plate. A small linear part was observed after this inflexion, followed by a slight non linearity when approaching the maximum load which corresponds to the critical load at failure.

Figure 8(b) plots the COD as a function of the deflection. By contrast to what was reported with the usual SENB geometry (Challier et al. 2006), non-linearities could be noticed in the relationship between the deflection and the COD. To go further, the evolution of the ratio of the deflection by the COD is plotted in Figure 8(c). A transient stage can be observed up to a deflection of 3 mm. This can be attributed to the gradual compression of the specimen in the beginning of the test. Then, between 3 mm and 8 mm approximately, this ratio exhibits either a stabilization at 11.5 for Specimen #3, or a very small decreasing rate for Specimen #1 and Specimen #2. The latter shows a good reproducibility and the average value of the ratio is estimated to be 8.

In the last part of the loading (from a deflection of 8 mm up to the failure), a continuous decrease of this ratio is observed, clearly highlighting a nonlinear relationship between the deflection and the COD.

These macroscopic measurements together with the COD allowed the calculation of respectively $\Gamma$ (Equation (2)) and $J_p/\eta_p$ (Equation (4)). Recall that $A(F, d)$ in Equation (2) and $A_t(F, \text{COD})$ in Equation (4) were numerically integrated over the loading: $\Gamma$ and $J_p/\eta_p$ depend on the loading step. Their critical values $\Gamma_c$ and $J_c/\eta_p$ have to be determined at the moment of the failure. It should be noted that for classical (*i.e.* non clampled) SENB specimen the COD is proportional to the deflection and the calibration factor is known. Therefore, the two load parameters, as well as their critical values differ by a fixed multiplier factor. The above mentioned

non linearities motivated further analysis concerning the material and specimen geometry under study.

Figure 9(a) shows a continuous increase of $\Gamma$ as a function of the deflection for the three specimens. While good agreement is obtained for Specimen #2 and Specimen #3, a large deviation

**Figure 9** Function of the deflection of (a) the fracture energy related to the net cross section area, (b) the J-integral related to $\eta$, and (c) the ratio between the two above mentioned parameters.
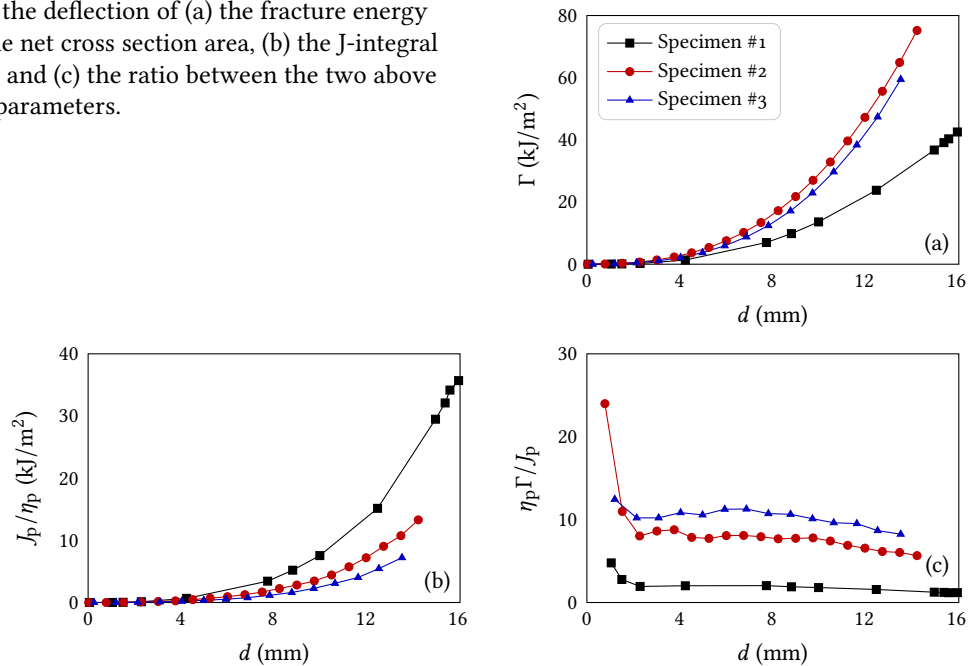


is observed for Specimen #1.

An attempt was then made to plot $J_p$, see Equation (4), with respect to the deflection. Since the calibration factor $\eta_p$ was unknown, the study focused on the reduced load parameter $J_p/\eta_p$ in Figure 9(b). The same conclusion as for $\Gamma$ can be drawn although the values were one order of magnitude lower.

Table 1 summarizes the values at failure of the characteristic parameters. A large scatter

| Specimens | $d$ (mm) | $F$ (N) | COD (mm) | $\Gamma_c$ (kJ/m$^2$) | $J_c/\eta_p$ (kJ/m$^2$) |
|---|---|---|---|---|---|
| #1 | 16.04 | 210.8 | 2.41 | 42.5 | 37.5 |
| #2 | 14.29 | 193.6 | 2.09 | 75.2 | 13.3 |
| #3 | 13.59 | 169.9 | 1.42 | 59.4 | 9.21 |

**Table 1** Values at failure of the collected experimental data together with the fractured surface energy density $\Gamma_c$ and fracture toughness $J_c/\eta_p$ calculated as the values at failure of $\Gamma$ and $J_p/\eta_p$, respectively.

could be observed in $\Gamma_c$ and $J_c/\eta_p$ in the two last columns. Furthermore, the scattered $\Gamma_c$ values significantly differed from the impact strength in the ductile plateau given in Figure 3: 0.25 kJ/m$^2$, $i.e$ by a factor 100. This is problematic from the mechanical engineering viewpoint. Indeed, $\Gamma_c$ is required for the design and the safety of the airbag window during the deployment.

Further analysis was carried out by focusing on the ratio of $\Gamma$ to $J_p/\eta_p$. In fact, from Equation (2) and Equation (4), this ratio can be expressed as

$$\frac{\eta_p \Gamma}{J_p} = \frac{\eta_p d}{\text{COD}}. \tag{5}$$

This ratio is a function of the unknown calibration factor $\eta_p$ and the ratio of the deflection to the COD plotted in Figure 8(c). Figure 9(c) shows the ratio $\eta_p\Gamma/J_p$ as a function of the deflection. As expected, the curve follows the same trends as that of $d/$COD in Figure 8(c). It should however be mentioned that $\eta_p$ depends on the crack depth ratio $a/W$. Therefore, for a *stationary* crack, its constant value can be deduced, allowing the determination of both $J_p$ and the multiplication factor between the impact strength and the fracture toughness.

By applying this methodology for the data in Table 1, *i.e.* at failure, $\eta_p$ was estimated to be 0.17, 0.83 and 0.67 respectively for Specimens #1, #2 and #3. This large scatter cannot be used as such in a mechanical engineering calculation for design and safety. Further investigation was carried out and developed in the following.

### 4.1.2 Crack extension

For the three specimens, the crack extension $\Delta a$ during the test is plotted with respect to the deflection in Figure 10(a). A key point arises from the curves altogether: the crack systematically
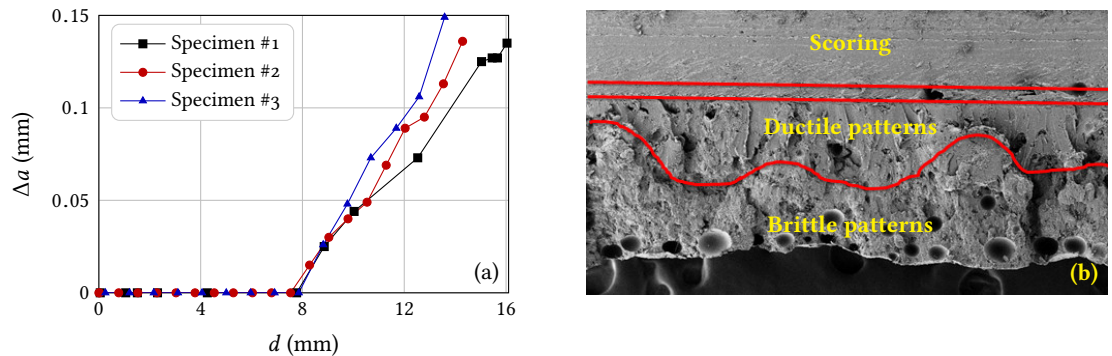


**Figure 10**  Information about the cracking. (a) Crack extension $\Delta a$ with respect to the deflection. (b) Representative SEM examination of the fracture surface.

initiated very early, at a deflection of about 8 mm, corresponding to a load of about 80 N, that is, less than half of the load at failure mentioned above. After this initiation, the crack progressed quasi-linearly as the deflection increased. The maximum crack extension measured at the lateral surface, just before the failure of the specimen, was about 0.15 mm. Figure 10(a) clearly evidences that the crack was not stationary: the depth ratio $a/W$ goes from 0.5 to 0.625 when the deflection runs from 8 mm to about 15 mm.

Fracture surface examinations were carried out by Scanning Electron Microscopy so as to analyse the through thickness crack extension. Figure 10(b) illustrates the main features observed on a representative fracture surface after the tests (with permanent set). The initial crack implanted by the robot (scoring) exhibited a specific fracture surface with some apparent striations due to the marks of the blade of the robot. Ahead of this pre-existing crack, an area surrounded by the two red straight lines showed some deformed fibrils that could be attributed to the blunting of the initial crack. This pattern was then followed by a rather flat surface with non-regular crack extension. This was considered as a ductile crack surface where the ductile crack propagation occurred. One can refer to Figure 7 to observe the side views of the blunting and the ductile crack extension. Beyond this latter, a more rugged surface, assumed to be a brittle pattern, appeared up to the end of the thickness. The deduced scenario could be summarized as follows, consecutively to increasing deflection:

- Blunting of the crack tip;
- Ductile crack initiation;
- Stable crack growth (ductile tearing);
- Rapid crack growth: this ultimate "brittle" failure did not have the same characteristics as that obtained at very low temperature. Indeed, this happened after the ductile tearing, thus, at a larger crack depth ratio and no fragmentation of the sample was observed.

The observed surface was not exactly at mid-thickness so that the average depth might be larger elsewhere. Several bubbles (voids/cavities), with an average diameter of about 0.05 mm, were observed on the fracture surfaces. Although their effects were not in the scope of this paper, it can be expected that their presence affected the reproducibility of the experimental data.

It can be deduced from these observations that the maximum load and the crack initiation did not coincide. The key experimental data at both crack initiation and the failure of the specimen are gathered in Table 2.

When using the fracture mechanics concepts, the curve to be analysed should be the load versus the COD. Following Hale and Ramsteiner (2001), a linear correction had to be operated so

| Specimens | $\Delta a$ (mm) | | $d$ (mm) | | $F$ (N) | | COD (mm) | |
|-----------|------|------|------|-------|------|-------|------|------|
| Events    | init. | fail. | init. | fail. | init. | fail. | init. | fail. |
| #1        | 0    | 0.14 | 7.77 | 16.04 | 84.9 | 210.8 | 0.91 | 2.41 |
| #2        | 0    | 0.14 | 7.53 | 14.29 | 82.4 | 193.6 | 0.89 | 2.09 |
| #3        | 0    | 0.15 | 7.86 | 13.59 | 76.3 | 169.9 | 0.71 | 1.42 |

**Table 2**  Key experimental data at the crack initiation and at the failure of the specimens.

as to prevent the effects of the non-linearity due to penetration of the loading pins into the sample. To this end, the stiffness—defined as the inverse of the compliance of the specimen—was calculated as the derivative, point by point, of the load with respect to the COD: $dF/d(COD)$. The stiffness as a function of the applied deflection is plotted in Figure 11(a) to Figure 11(c), superimposed with the evolution of the crack extension, corresponding to the second $Y$-axis. Two significant conclusions could be deduced from these curves.

**Figure 11**  Decrease of the stiffness correlated to the increase of crack extension for (a) Specimen #1, (b) Specimen #2, and (c) Specimen #3.
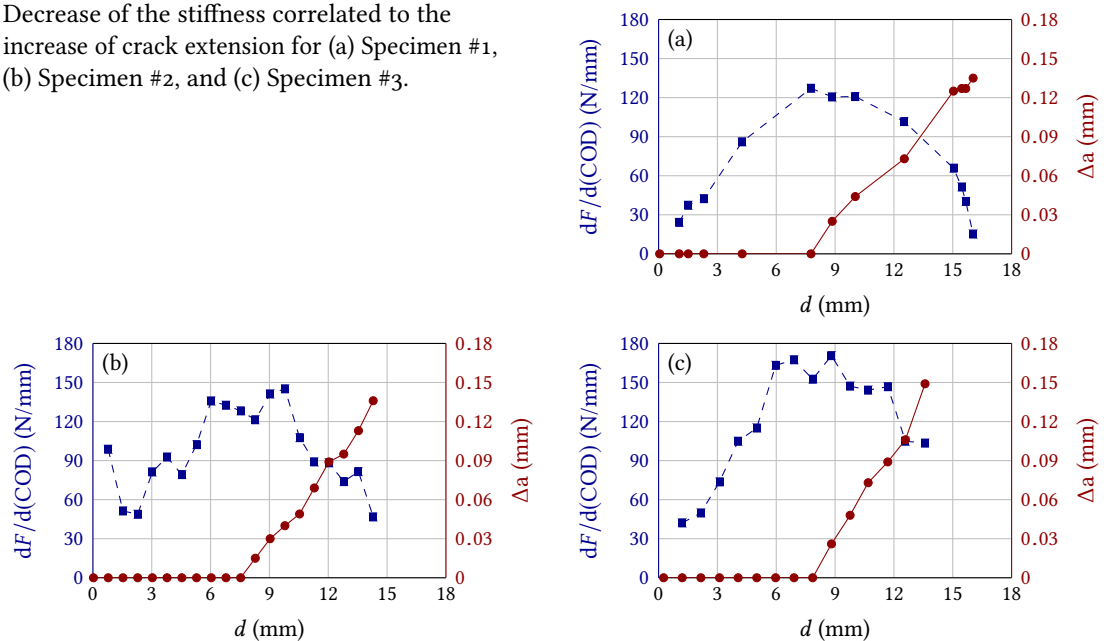


- In contrast to the classical SENB data, the linear correction affected a larger part of the load versus COD curve. There was no plateau of the stiffness corresponding to the elastic compliance of the curve.
- The stiffness decreased as soon as the crack extension started to progress; meaning that the non linearity in the load versus COD curve was essentially due to the crack initiation and growth, but not to the plasticity.

  In order to prepare for fracture mechanics concepts to be applied, namely using FE analysis, the same key curves as in Figure 8 and Figure 9 are plotted as a function of the COD in Figure 12, with linear correction. Figure 12(a) displays the load versus COD curves showing the corrected linear part. The stiffness was estimated to be $(140 \pm 20)$ N/mm. The last experimental points corresponding to the failure of the specimens, a large scatter could be observed concerning the COD at failure. Especially, the curve of Specimen #3 had a small COD at failure in comparison with the two others. As mentioned above, the trend of the crack extension as a function of the COD in Figure 12(b) shows stable growth of about 0.15 mm before the abrupt failure: the crack depth ratio a/W evolved from 0.5 to 0.625. Again, Specimen #3 showed a steeper slope meaning a more brittle failure. The solid red line in Figure 12(b) illustrates a fit of the crack extension of Specimen #2. This was used as boundary condition for the FE release nodal degree of freedom technique. The knowledge of the crack extension allowed the calculations of $J_p/\eta_p$ (Equation (4)) by updating the actual crack depth. In Figure 12(c), after correction of the linear part, $J_p/\eta_p$ is plotted as a function of the COD. These curves show less scatter and smaller values of $J_p/\eta_p$ than in Figure 9(b).

**Figure 12**    (a) Load $F$, (b) crack extension $\Delta a$, and
(c) J-integral related to $\eta_p$ with respect to COD.
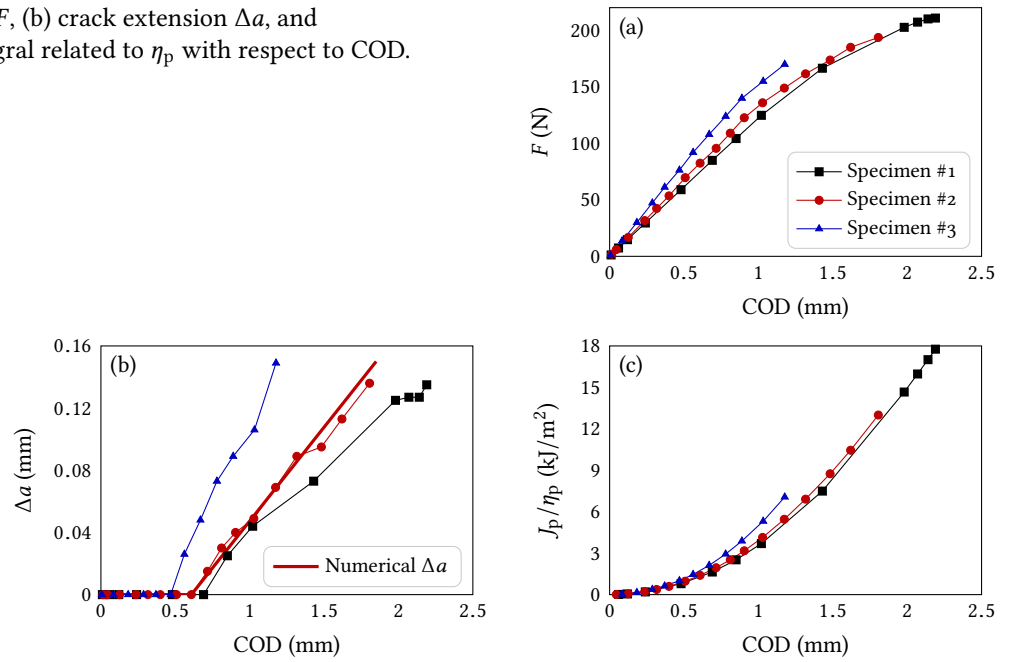


Table 3 displays the characteristic values of the main mechanical parameters obtained experimentally followed by the corresponding $J_p/\eta_p$. Apart from Specimen #3, $J_p/\eta_p$ at crack

| Specimens | $\Delta a$ (mm) | | COD(mm) | | $F$ (N) | | $J_p/\eta_p$ (kJ/m$^2$) | |
|---|---|---|---|---|---|---|---|---|
| Events | init. | fail. | init. | fail. | init. | fail. | init. | fail. |
| #1 | 0 | 0.14 | 0.69 | 2.19 | 84.9 | 210.8 | 1.64 | 17.8 |
| #2 | 0 | 0.14 | 0.61 | 1.81 | 82.4 | 193.6 | 1.40 | 13.0 |
| #3 | 0 | 0.15 | 0.47 | 1.18 | 76.3 | 169.9 | 1.01 | 7.06 |

**Table 3**    Load parameter $J_p/\eta_p$ calculated from experimental data after linear correction of the COD.

initiation was 10 times less than at failure. Specimen #2 data set was selected for the FE simulation of propagating crack. Indeed, specimen #3 was mentioned to exhibit some deviation compared with the two others; whereas Specimen #1 showed a peculiar crack growth behaviour at the onset of the failure (see black full square in Figure 12(b)).

## 4.2    Finite Element simulations

The purpose of the FE simulations was essentially to numerically compute the J-integral load parameter so as to compare it with that of Equation (4). The J-integral being dependent on the crack depth, three specific conditions were simulated:
- a stationary crack with the initial crack depth $a_0$,
- a stationary crack with the ultimate crack depth $a_f$, and
- a propagating crack from $a_0$ to $a_f$.

Furthermore, the release nodal degree of freedom (rndof) technique was assigned to follow the fit of the crack extension in Figure 12(b).

### 4.2.1    Inverse optimization of the material parameters

Before computing the J-integral load parameter, the material parameters were determined by using inverse method of optimization in the Z-set suite. This optimization was performed using the load versus COD with the propagating crack. Therefore, the simulated curve—to be compared with the experimental one—accounted for the crack growth using the rndof technique. A simple elasto-plastic model was used during the optimization.

Figure 13(a) illustrates the comparison of the experimental with the simulated load versus COD curves, obtained from the optimized material parameters. The oscillations observed in the simulation response were due to the discrete crack growth applied on the three isoparametric elements ahead of the crack tip.

**Figure 13**   (a) Load versus COD for various configurations. Opening stress contour map on the deformed crack tip (b) at the end of the linear part and (c) at the end of the ducile crack growth.
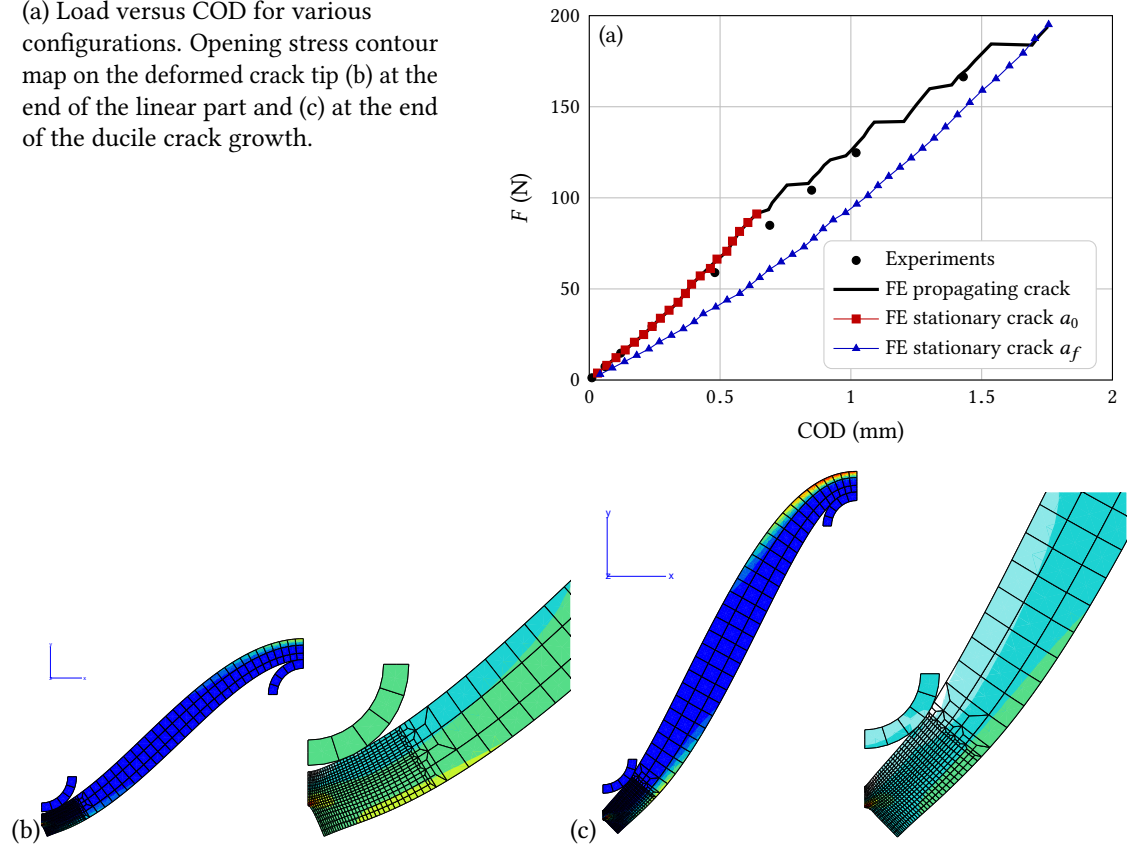


Figure 13(b) and Figure 13(c) show the opening stress contour map on the deformed specimen (left) and the deformed crack tip (right), respectively at the onset of crack initiation (crack depth = $a_0$) and at the onset of the brittle failure, that is, at the end of the ductile crack propagation leading to a crack depth of $a_f$.

Note that the remaining ligament $(W - a_0)$ in Figure 13(b) is longer than $(W - a_f)$ in Figure 13(c). This indicates that the numerical crack growth was actually operated. Furthermore, the impactor was observed to detach from the top of the PVC specimen at these loading steps. This phenomenon is also experimentally observed—even though not very clearly—in Figure 7.

Once the material parameters were obtained, two simulations with stationary cracks ($a_0$ and $a_f$) were carried out so as to compare the compliance of the system, see Figure 13(a).

- Red full square symbols correspond to the crack depth $a_0$. Obviously, the load versus COD was in line with that of the propagating crack. Moreover, this curve was linear, meaning that linear fracture mechanics concept should be valid before the crack initiation;

- Blue full triangles represent the crack depth $a_f$. The compliance was clearly larger (lower stiffness) due to larger crack depth. The end of the load versus COD showed a slight hardening, that probably was due to the contact configuration in Figure 13(b) and Figure 13(c). However, the last point coincided with the propagating crack simulation.

### 4.2.2   Fracture toughness & Elastic calibration factor

The Z-set finite element code is provided with a routine allowing numerical J-integral to be computed using the de Lorenzi method (de Lorenzi 1982). For common fracture mechanics specimens such as SENB or CT, the numerical J-integral is correlated with $J_p$ if the experimental and numerical load versus COD curves are in good agreement, as this is the case in Figure 13(a). Therefore the FE J-integral, noted $J_{FE}$, was assumed to be reliable for the clamped SENB specimen.

Seven $J_{FE}$ were requested to the Z-set code according to the crack progress: at the initial crack depth ($a_0$), then at each crack extension of 25 µm until the final crack depth prior to failure ($a_f$). The stabilization of $J_{FE}$ was checked thanks to eight rows of elements surrounding each of the seven crack tips. Typically, it was obtained from the second or the third row of elements. Of course, if the crack tip did not correspond to that of the rndof procedure, the computed $J_{FE}$ at this location was ignored.

In Figure 14, the seven values of $J_{FE}$ are plotted with respect to the COD as black full square symbols. The blue full circle symbols were attributed to the "experimental" $J_p/\eta_p$.

**Figure 14**  J-integral related to $\eta_p$ as a function of the COD.
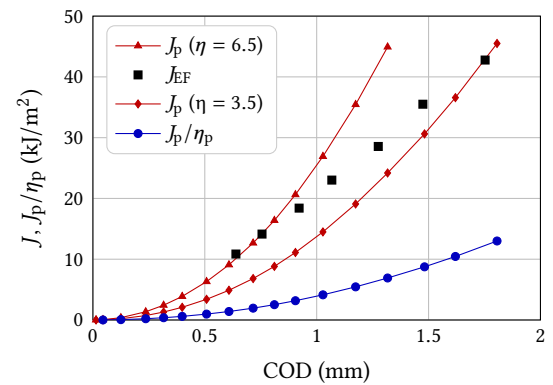


The determination of the fracture toughness requires the load versus COD curve so as to calculate J-value and the corresponding crack extension $\Delta a$. As pointed out by Baldi et al. (2013), a clear transition from the crack blunting phase to the fracture propagation is not easy to observe, especially for 3D crack shape in opaque polymers. It is often proposed to take, either the J-value at the maximum load or the J-value at a given amount of crack extension (0.2 mm for instance). In the present work, the fracture toughness $J_c$ was assumed to be the value of $J_{FE}$ at the crack initiation. From Figure 14, it was estimated to be $10.8\,kJ/m^2$. This value is very close to that obtained by Hale and Ramsteiner (2001) for a modified PVC: $J_{0.2} = 10.2\,kJ/m^2$.

Once the fracture toughness obtained, the evaluation of the calibration factor was attempted by using the value of $J_p/\eta_p = 1.4\,kJ/m^2$ at crack initiation for Specimen #2 in Table 3. The calculation allowed an estimate of $\eta_p \approx 8$ for the clamped SENB with $a/W = 0.5$, at least for the plasticized PVC under study. The following should be mentioned.

- This value is four times higher than that of a classical (non clamped) SENB specimen.
- By considering Equation (3) and Figure 13(a), where the load versus COD is linear up to the crack initiation, it could be assumed that the obtained calibration factor was actually the elastic one $\eta_e$. Indeed, at this stage, $A_p(F, COD) = 0$ and $A_e(F, COD)$ corresponds to the area of the triangle $(0, F, COD)$ at the crack initiation.
- The fracture toughness $J_c = 10.8\,kJ/m^2$ should be used for the prediction of the crack initiation on engineering structures. Especially, on CEAST scored specimens tests (Bertaux et al. 2021), on the one hand, and on the window of the airbag box located in the dashboard, on the other hand. As soon as the J-integral can be computed or calculated, the prediction consists of a comparison between the value of J-integral with $J_c$.

### 4.2.3  Crack propagation

Once the crack had initiated, the next experimental points dealt with crack growth ($\Delta a \neq 0$). The load versus COD curve exhibited non linearity. In strict logic, this implies to separate the two calibration factors $\eta_e$ and $\eta_p$ in Equation (3), themselves depending on the crack depth ratio. To overcome this difficulty, the use of Equation (4) was proposed here. The evolution of $\eta_p$ as a function of $a/W$ was determined by using the total area under the load versus COD curve. To this end, a multiplicative factor was attributed to each of the six remaining $J_{FE}$ in Figure 13(a), so as for the "experimental" $J_p/\eta_p$ curve to intersect this point. The red curves with triangle and diamond symbols in Figure 14 examplified this approach for, respectively, the second and the last $J_{FE}$ values. These multiplicative factors are plotted as a function of the crack depth ratio in Figure 15. A linear evolution of the $\eta_p$ calibration factor could then be established, allowing an access to the J-integral by using Equation (4) whatever the crack depth ratio.

Taking advantage of $J_{FE}$ associated with $\Delta a$, an attempt was made to establish the crack growth resistance (R) curve of the studied plasticized PVC. The testing protocol for conducting J-crack growth resistance curve tests on plastics consists of using multiple specimens with various crack depths (Hale and Ramsteiner 2001). Recent works carried out under the direction of the Technical Committee 4, "Polymers, Polymer Composites and Adhesives," of the European

**Figure 15**　Calibration factor $\eta_\mathrm{p}$ as a function of the crack depth ratio $a/W$.
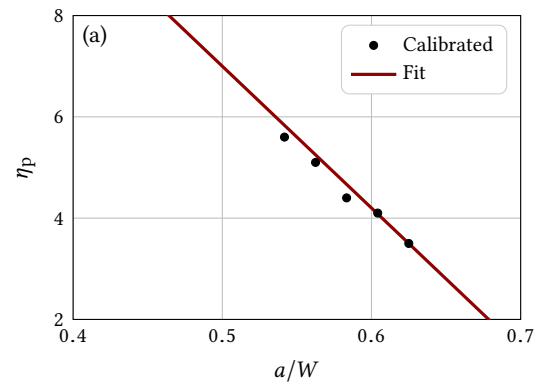


Structural Integrity Society (ESIS TC4) suggested the use of two specimens so as to obtain the R-curve (Agnelli et al. 2015; Baldi et al. 2020). The following results represent a contribution to this active work on fracture of plastics.

Figure 16 displays $J - \Delta a$ from Specimen #2 data assisted by FE analysis. The six points allow

**Figure 16**　Resistance R-curve ($J - \Delta a$ curve) of the PVC material under study.
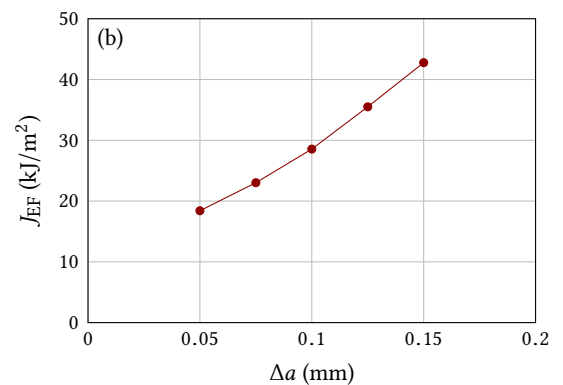


the prediction of the ductile crack growth in this material on a small amount of crack extension. However, when attempting to plot the blunting line, it was far below this $J - \Delta a$ curve. This blunting assumed to be semi-circular (Williams 2001) theoretically can be estimated to be half of the crack tip opening displacement. As mentioned above, Figure 7 showed a large blunting of the crack tip. This result could have been expected. Further assessment should be carried out before using safely the present $J - \Delta a$ curve.

## 5　Discussion

This section focuses on the methodology allowing the transferability (Brocks et al. 1989) of the clamped specimen results, in terms of crack initiation and propagation, into the CEAST tests first and by extension to the dashboard. A major assumption should be outlined here: the temperature and the impact speed selected locate the test in the upper shelf of the fracture toughness curve. The ductile mechanisms operate and $J_\mathrm{c} = 10.8\,\mathrm{kJ/m^2}$ and the R-curve are considered to be valid.

### 5.1　From clamped SENB to CEAST test results

Recall that the geometries of the impactors were circular (round bar) and hemispherical for the clamped SENB and the CEAST tests, respectively. The mechanisms of crack initiation and growth differed in the portion of process zone in the remaining ligament. Whereas for clamped SENB the whole width (29.8 mm) was involved, in the CEAST specimen the sequence was as follows:

- when the impactor tip entered in contact with the top surface of the sample at the end of the remaining ligament, only a small portion of the diameter $\Phi$ of the impactor was concerned with the crack initiation;
- this initiated crack propagated through the thickness;
- the displacement of the hemispherical impactor induced lateral crack propagation, *i.e.* perpendicular to the direction of the impactor displacement.

The approach should be based on the crack initiation, *i.e.* as soon as $J_c = 10.8\,\text{kJ/m}^2$ is reached. For CEAST tests, only the load versus deflection was available. For mechanical engineering purpose, namely the safety engineering design of structures, the salient question is how to determine the ductile crack initiation from these data.

By using a FE code, the approach consists of computing the J-integral on the meshed CEAST specimen using an elastic-visco-plastic model. The experimental load versus deflection curve should be in agreement with the simulated one at each test temperature and impact speed. When the J-integral reaches the fracture toughness value $10.8\,\text{kJ/m}^2$, the crack initiation is supposed to be established and the computation should be stopped.

The analytical approach is more complex. Recall that at the crack initiation for clamped SENB specimens, the load versus COD curve is linear so that, on the one hand, the calibration factor is equal to the elastic one ($\eta_e \approx 8$); on the other hand, Figure 8(c) indicates that the deflection of about 8 mm is proportional to the COD.

Since the crack initiation was detected at the COD where the stiffness (inverse of the compliance) decreased, it should be also valid for the stiffness in terms of load versus deflection curve. This operation was carried out directly on the data of the CEAST tests in Figure 2. For the three tests, the stiffness increased first up to a deflection of 8 mm, then stabilized between 8 mm and 10 mm to decrease at last. The crack initiation was assumed to occur at 10 mm for CEAST tests at 23 °C and 4.4 m/s. To go further, the energy $A(d = 10\,\text{mm})$ according to Equation (1) is equal to $(2.0 \pm 0.1)\,\text{J}$. This energy should be related to the fractured surface used to the determination of the impact strength $\Phi(W - a_0)$, giving $0.11\,\text{kJ/m}^2$. This value is twice lower than the upper shelf impact strength in Figure 3 ($0.25\,\text{kJ/m}^2$). But, it corresponds to the actual crack initiation, in agreement with the fracture toughness of the material. This "impact strength at crack initiation" should be assessed by using all the CEAST experimental data:

- by determining the deflection from which the stiffness decreases,
- by integrating the area under the load versus deflection curve up to the selected deflection, so as to estimate the energy at crack initiation, and
- by relating this energy to the area of the remaining ligament assumed to be $\Phi(W - a_0)$.

## 5.2   From CEAST results to the full scale test on dashboard

For a real engineering structure like the dashboard, only FE analysis would be efficient for the prediction of the crack initiation to allow the correct deployment of the air bag. To this end, the window of the air bag box, see Figure 1, should be meshed in detail. The three layers of materials as well as the scoring in the PVC skin should be discretized with sufficiently refined meshes. The challenge is to reduce the numerical cost of such a study.

The same material parameters of elasto-visco-plastic model that have been identified for the CEAST tests at the temperatures and impact speeds located in the upper part of the diagram of Figure 4 should be used.

The boundary conditions should be associated to the kinetic energy due to the air bag deployment. The safe opening of the window, in ductile mechanisms, corresponds to the precise conditions (time, temperature, loading...) allowing the J-integral to reach the fracture toughness of the material.

Once this goal is achieved, many parameters of interest can be optimized to ensure a safe deployment of the air bag:

- the formulation and the processing of the material to obtain an efficient time and temperature dependent constitutive model;
- the drawing of the scoring as straight line, Y or U or L shaped that already exist;
- the score depth ratio as it was shown that for 0.625 a net brittle failure, without branching or fragmentation of the skin, occurred;
- the kinetic energy due to the air bag display.

## 6   Concluding remarks

The desired fracture process allowing the safety of the passengers during the deployment of the airbag in automotive industry is the ductile failure. Full scale experiments on dashboard showed

that the impact speed was estimated to be 25 m/s and at 23 °C, a ductile failure of the skin—made of plasticized PVC—was evidenced. This result was in agreement with the domain of temperatures and impact speeds established with drop tower tests at lower speeds/temperatures (Bertaux et al. 2021).

Dedicated clamped SENB specimens were used to characterize the mechanisms of ductile crack initiation and propagation for the studied material. In contrast to the route recommended by non linear fracture mechanics, the crack initiation occurred before the maximum load prior to the final failure of the specimen. In fact, it was observed when the loss of linearity in the load versus COD appeared. Thanks to the "release nodal degree of freedom" procedure, the in-house FE code allowed the simulation of the crack extension to be performed. The calibration factor of the clamped SENB specimen with respect to the crack depth ratio was established. Moreover, the fracture toughness $J_c$, defined as the numerical J-integral at the crack initiation, was evaluated to be 10.8 kJ/m$^2$, in agreement with values reported in the literature.

Focusing on the crack initiation, the corresponding impact strength for the previous drop tower tests in the upper shelf was corrected. Instead of the previous 0.25 kJ/m$^2$ this critical value was reduced to 0.11 kJ/m$^2$. The modified fracture toughness and the impact strength values were proposed in the methodology allowing the ductile crack initiation to be predicted.

- For the drop tower test results where the COD and the crack extension were not available. Two methods were proposed:
    - by running FE analysis of the test and selecting the time when the J-integral reached the value of 10.8 kJ/m$^2$, and
    - by detecting the loss of linearity in the load versus deflection curve for which the fractured surface energy density was equal to 0.11 kJ/m$^2$.
- For the dashboard where the plasticized PVC skin was integrated. Once the whole structure was meshed, FE simulation of the airbag display should be performed up to the time when the numerical J-integral reached the value of 10.8 kJ/m$^2$.

It was mentioned that using FE code would allow the optimization of many parameters to lead to a safe deployment of the air bag.

## References

Agnelli, S., F. Baldi, B. R. K. Blackman, L. Castellani, P. M. Frontini, L. Laiarinandrasana, A. Pegoretti, M. Rink, A. Salazar, and H. A. Visser (2015). Application of the load separation criterion in J-testing of ductile polymers: A round-robin testing exercise. *Polymer Testing* 44:72–81. [DOI], [OA].

ASTM D6110-18 (2018). *Standard Test Method for Determining the Charpy Impact Resistance of Notched Specimens of Plastics*. Norm. West Conshohocken, PA: ASTM International. [DOI].

Baldi, F., S. Agnelli, L. Andena, B. Blackman, L. Castellani, P. Frontini, J. Kučera, L. Laiarinandrasana, A. Pegoretti, A. Salazar, and L. Warnet (2020). Determination of the Fracture Resistance of Ductile Polymers: The ESIS TC4 Recent Experience. *Materials Performance and Characterization* 9(5):675–687. [DOI], [HAL].

Baldi, F., S. Agnelli, and T. Riccò (2013). On the determination of the point of fracture initiation by the load separation criterion in J-testing of ductile polymers. *Polymer Testing* 32(8):1326–1333. [DOI].

Bertaux, C., N. Amouroux, C. Ovalle-Rodas, and L. Laiarinandrasana (2021). Impact speed dependency of the ductile failure threshold temperature for a plasticized Polyvinylchloride. *Continuum Mechanics and Thermodynamics*. [DOI], [HAL].

Bohme, W. and H. J. MacGillivray (1996). Experience with instrumented Charpy tests obtained by a DVM round-robin and further development. *Evaluating Material Properties by Dynamic Testing ESIS 20*. Mechanical Engineering Publications, pp 1–23.

Brocks, W., G. Künecke, H.-D. Noack, and H. Veith (1989). On the transferability of fracture mechanics parameters from specimens to structures using fem. *Nuclear Engineering and Design* 112:1–14. [DOI].

Bulloch, J. H. (2004). A study concerning material fracture toughness and some small punch test data for low alloy steels. *Engineering Failure Analysis* 11(4):635–653. [DOI].

Challier, M., J. Besson, L. Laiarinandrasana, and R. Piques (2006). Damage and fracture of polyvinylidene fluoride (PVDF) at 20 °C: Experiments and modelling. *Engineering Fracture Mechanics* 73(1):79–90. [DOI], [HAL].

Cox, K. R. and R. E. Robertson (2007). Controlling Failure of Polymer Skin/Foam Bilaminate Sheets. *2007 SAE World Congress* (Detroit, USA). SAE International. [DOI], [HAL].

Hale, G. E. and F. Ramsteiner (2001). J-Fracture toughness of polymers at slow speed. *Fracture Mechanics Testing Methods for Polymers, Adhesives and Composites*. Vol. 28. European Structural Integrity Society. Elsevier, pp 123–157. [DOI], [HAL].

ISO 179-1:2010 (2010). *Plastics — Determination of Charpy impact properties — Part 1: Non-instrumented impact test*. Norm. Geneva, CH: International Organization for Standardization. [URL].

ISO 6603-2:2000 (2000). *Plastics — Determination of puncture impact behaviour of rigid plastics — Part 2: Instrumented impact testing*. Norm. Geneva, CH: International Organization for Standardization. [URL].

Laiarinandrasana, L., M. R. Kabiri, and M. Reytier (2006). Effect of specimen geometries on the $C^*$ versus d$a$/d$t$ master curve for type 316L stainless steel. *Engineering Fracture Mechanics* 73(6):726–737. [DOI], [HAL].

Laiarinandrasana, L., Y. Nziakou, and J. L. Halary (2012). Fracture behavior of amorphous and semicrystalline blends of poly(vinylidene fluoride) and poly(methyl methacrylate). *Journal of Polymer Science Part B: Polymer Physics* 50(24):1740–1747. [DOI], [HAL].

de Lorenzi, H. G. (1982). On the energy release rate and the J-integral for 3-D crack configurations. *International Journal of Fracture* 19(3):183–193. [DOI], [HAL].

Macgillivray, H. J. (2001). J-Fracture toughness of polymers at impact speed. *Fracture Mechanics Testing Methods for Polymers, Adhesives and Composites*. Vol. 28. European Structural Integrity Society. Elsevier, pp 159–175. [DOI].

Marcellan, A., A. Bunsell, R. Piques, and L. Laiarinandrasana (2019). In Situ tensile tests to analyze the mechanical response, crack initiation, and crack propagation in single polyamide 66 fibers. *Journal of Polymer Science Part B: Polymer Physics* 57(11):680–690. [DOI], [HAL].

Tanguy, B., C. Bouchet, S. Bugat, and J. Besson (2006). Local approach to fracture based prediction of the $\Delta \mathcal{T}_{56J}$ and $\Delta T_{K_{Ic,100}}$ shifts due to irradiation for an A508 pressure vessel steel. *Engineering Fracture Mechanics* 73(2):191–206. [DOI], [HAL].

Williams, J. G. (2001). $K_c$ and $G_c$ at slow speeds for polymers. *Fracture Mechanics Testing Methods for Polymers, Adhesives and Composites*. Vol. 28. European Structural Integrity Society. Elsevier, pp 11–26. [DOI], [HAL].